Thin film and bulk morphology of PI-PS-PMMA miktoarm star terpolymers with both weakly and strongly segregated arm pairs

Ariaee, Sina; Jakobsen, Bo; Norby, Poul; Smilgies, Detlef-M.; Almdal, Kristoffer; Posselt, Dorthe

Published in:
Polymer

Link to article, DOI:
10.1016/j.polymer.2023.126202

Publication date:
2023

Document Version
Publisher's PDF, also known as Version of record

Polymer 283 (2023) 126202

Contents lists available at ScienceDirect

Polymer

journal homepage: www.elsevier.com/locate/polymer

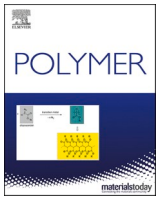

Thin film and bulk morphology of PI-PS-PMMA miktoarm star terpolymers with both weakly and strongly segregated arm pairs

Sina Ariaee [a], Bo Jakobsen [a], Poul Norby [c], Detlef-M. Smilgies [d], Kristoffer Almdal [b], Dorthe Posselt [a,*]

[a] IMFUFA, Department of Science and Environment, Roskilde University, Universitetsvej 1, P.O Box 260, 4000, Roskilde, Denmark
[b] Technical University of Denmark, DTU Chemistry, Kemitorvet 206, 2800, Lyngby, Denmark
[c] Technical University of Denmark, Department of Energy Conversion and Storage, Fysikvej 310, 2800, Lyngby, Denmark
[d] Cornell High Energy Synchrotron Source (CHESS), Cornell University, Ithaca, NY, 14853, USA

ARTICLE INFO

Keywords:
Living anionic polymerization
ABC miktoarm star terpolymer
Self-assembly
Bulk morphology
Thin film morphology
X-ray reflectometry (XRR)
Small angle X-ray scattering (SAXS)
Transmission electron microscopy (TEM)
Scanning electron microscopy (SEM)
Atomic force
Microscopy (AFM)

ABSTRACT

A series of three homologous ABC miktoarm star terpolymers having a polyisoprene (PI), a polystyrene (PS) and a poly(methyl methacrylate) (PMMA) arm, is synthesized by living anionic polymerization. While the volume fraction of the PI and the PS blocks are kept equal and constant, the volume fraction of the PMMA block is varied. The room temperature bulk structure is characterized using small-angle X-ray scattering and transmission electron microscopy, while the structure of thin films is investigated using scanning electron microscopy, atomic force microscopy and X-ray reflectometry. For both bulk and thin films, it is found that the sample with the lowest volume fraction of PMMA has a morphology distinctly different from the two samples with larger PMMA volume fraction. All data for both bulk and thin film samples are consistent with an alternating lamellar structure for the lowest PMMA volume fraction sample. The two higher PMMA volume fraction samples show standing rod structure, however the details of the packing in the PMMA matrix differ depending on sample thickness. Overall, a structure with PI domains screened from interacting with PMMA by a PS shell is seen for both samples. In bulk, core-shell cylinders pack hexagonally, while a 100 nm thin film of the sample with the largest volume fraction of PMMA shows a square-lattice packing. The structuring is driven by two factors: i) the strong segregation of the PI-PMMA arm pair together with the weak segregation of the two arm pairs with a PS block and ii) the geometrical constraints resulting from the star architecture. No wetting layers are observed for any of the thin film samples, neither at the air-polymner surface or at the polymer-substrate interface.

1. Introduction

Block copolymers (BCPs), where two or more chemically different polymer chains are linked together, can self-assemble into nanoscale ordered structures [1–4]. BCPs with long-range order have a host of potential applications, e.g. as nanolithography and patterning templates [5–14], as etch resistant scaffolds [15], in nanofabrication [16], as guides for nano-patterning graphene [17], as separation membranes for water purification [18,19], in electronic packaging [20], in drug delivery [21], and in solar cell industries [22].

The architecture of BCPs with three polymer blocks joined together (tri-BCPs) can be categorized as linear or branched. Specifically, when the three blocks are joined at a common point, a star terpolymer is formed [23]. Such a star terpolymer is labeled an ABC miktoarm star terpolymer (in the following ABC star) if the three blocks are chemically different [24].

In the case of ABC stars, the addition of a third block to a single junction point increases the complexity of the system in terms of synthesis, in terms of the governing parameters of self-assembly and also in the potential richness of the phase diagram [25–28]. For these systems, the equilibrium morphology is not only controlled by the volume fractions of the different components, f, the overall degree of polymerization, N, and the segmental interactions, χ, between the blocks (Flory-Huggins interaction parameter), the main governors for structurally simpler BCPs, but also by a more restricted confinement of the junction points [24]. Comparing the confinement of the junction points between linear tri-BCPs and the corresponding system with star architecture, the junction points of the former are located on planar

* Corresponding author.
E-mail address: Dorthe@ruc.dk (D. Posselt).

https://doi.org/10.1016/j.polymer.2023.126202
Received 30 March 2023; Received in revised form 7 July 2023; Accepted 17 July 2023
Available online 18 July 2023

interfaces, while the latter are located on lines [29,30]. This restriction can play an important role in structuring processes. As a result, for ABC star architecture, a host of different morphologies not found with simpler BCP architecture, i.e., tessellated, knitted or tiled morphologies is predicted [31–40].

In thin films with soft confinement (a thin film on a substrate), where interfacial interactions with the substrate and with air are introduced, additional constraints are placed on the possible ABC star morphologies. Furthermore, the overall film thickness, and its possible incommensurability with the characteristic domain spacing are players in defining the morphology. Hence, the self-assembly process in the films prepared with star architecture polymers as in the present study is generally complex and needs more studies [38–43]. In some cases, it has been found that the morphologies in thin films are different from the bulk counterparts [41,42].

In terms of theoretical studies on ABC stars, focus has been on bulk behavior, i.e. the effects of different arm volume fractions for equal segmental interactions [32,35,37,44–48] or the influence of different segmental interactions [31,42] on the morphology. Monte-Carlo simulations, dissipative particle dynamics (DPD) and self-consistent field theory (SCFT) have been utilized to predict the morphologies [31,33,37,49–52].

Fujimoto and coworkers were one of the first groups to investigate ABC stars composed of three incompatible arms of polydimethylsiloxane, polystyrene, and poly(*tert*-butyl methacrylate) experimentally and according to their work, the junction points are indeed confined to a line [28]. Takano and coworkers investigated a star architecture composed of polyisoprene (PI), polystyrene (PS), and poly (2-vinylpyridine) arms [53–56], where they reported honeycomb-type morphologies.

Hadjichristidis and coworkers were the first group to investigate the bulk morphologies of ABC stars comprised of PS, PI, and poly(methyl methacrylate) (PMMA) blocks using small-angle X-ray scattering (SAXS) and transmission electron microscopy (TEM) [57–59]. They had chosen a synthesis scheme resulting in large macromolecules in order to obtain high segregation strength, i.e., large values of χN. According to their observations, the samples self-assemble into columnar structures embedded in a PMMA matrix with PI as the core surrounded by a shell of PS. The shapes of the columns depend on the arm length ratio; cylinders for large PMMA blocks and diamond prisms for short PMMA block length. The authors also found the junction points to be located at lines where the three types of microdomain interfaces intersect [58].

Despite the advances in understanding the morphology of some ABC stars, a full characterization of various morphologies in both bulk and in thin films using electron microscopy and X-ray scattering techniques remains a challenge. TEM and scanning electron microscopy, SEM, are limited to examining the local morphology within an area of several square micrometers both in bulk and in thin films. Moreover, electron microscopy images, due to the electron beam penetration, are not always likely to reveal the presence of any wetting layers in thin films [60]. For SAXS, on the other hand, interpretation of the scattering pattern requires careful assessment of the individual contributions from the three different components, especially with low and varying electronic contrast between different constituent blocks as in the present case. This will be even more challenging when the intensity of the characteristic peaks decreases due to broad microdomain boundaries for weakly segregated blocks. Further understanding of the self-assembly process of ABC stars in thin films and the possible impact of surface energy contributions to restructuring are accessible by acquiring more information directly from top layers and from buried layers via atomic force microscopy (AFM) and X-ray reflectometry (XRR), respectively.

In this study, we present synthesis and characterization of a homologous series of ABC stars containing a mixture of weakly and strongly segregated PS, PI, and PMMA arms. A system with the same blocks has been investigated in Refs. [57–59]; however, in the present paper, an alternative synthesis scheme for the system is demonstrated to obtain star systems with lower N, i.e., lower segregation strength, χN. The PS and the PI block lengths are kept constant, while the PMMA arm length is varied. PI: PS: PMMA arm length ratios of 1:1:2.2 (ISM2.2), 1:1:3.7 (ISM3.7), and 1:1:5.4 (ISM5.4), were synthesized – in the following referred collectively to as ISM stars. In addition to bulk studies, we investigated thin film morphologies to shed light on the effect of surface interactions on the self-assembly process. We utilized SAXS and TEM for bulk morphological studies, and XRR, AFM and SEM for investigating the thin film structures.

2. Materials and methods

Chemicals were purchased from Sigma-Aldrich. Tetrahydrofuran (THF), cyclohexane and methyl methacrylate were purified and ISM stars synthesized using anionic polymerization realized according to Ndoni et al. [61] and shown in Scheme 1. 1,4-bis-(1-phenylethenyl)benzene (1,4-PEB) was obtained following Chernyy et al. [42]. Molar mass and molar mass distribution were characterized using a gel permeation chromatography (GPC) system comprising a Shimadzu LC-10AD pump, a SIL-10AD auto injector, three columns - guard, 300 × 8 mm^2 PLgel Mixed-C, 300 × 8 mm^2 PLgel Mixed-D - and a Viscotek model 200 combined viscosity and DRI detector. THF containing 1% trimethylamine was used as eluent at 0.5 ml/min flow rate.

Isoprene - see Scheme 1 - was polymerized using *sec*-butyllithium as initiator in cyclohexane for 10 h at 40 °C (caution: *overpressure*) resulting in poly(1,4-isoprene) [PI] (microstructure 75% *cis*-1,4, 20% *trans*-1,4, 5% 3,4) [62,63]. The living PI-Li was transferred to a reactor containing twofold excess with respect to polyisoprenyllithium of dry 1,4-PEB in THF and stirred for 8 h at −15 °C (deep blue color). The reaction mixture was precipitated into methanol and excess of 1, 4-PEB was removed by re-precipitation from THF in methanol. The resulting macromonomer, diphenylethylene terminated polyisoprene (PI-DPE) was dried at 60 °C until ca. 0.001 mbar. In the second step, styrene was polymerized in cyclohexane using sec-butyllithium as initiator for 5 h at 30 °C and the obtained PS-Li was transferred to the THF solution of PI-DPE macromonomer and stirred for 5h at −75 °C (intense red color). In the third step, a predetermined amount of methyl methacrylate (MMA) was added followed by withdrawal of an aliquot (ISM2.2) after 1 h at −75 °C. The MMA addition was repeated two more times (ISM3.7, ISM5.4) resulting in formation of in total three ISM miktoarm stars with varying molecular weight of the PMMA arm. The product was precipitated in methanol and dried under vacuum at 50 °C until ~0.001 mbar pressure was reached. Excess of unreacted PS and/or PI-DPE was removed by extraction with cyclohexane. NMR was performed using a Bruker AVANCE 400 MHz instrument. The integrated ^{1}H NMR (CDCl3, 400 MHz) peak intensities were utilized in order to estimate the mole fractions of the constituent blocks (i.e. PI, PS, and PMMA), which was then converted to the volume fractions of PI, PS and PMMA in the obtained ISM star polymers, as is listed in Tables 1 and 2. NMR spectra,

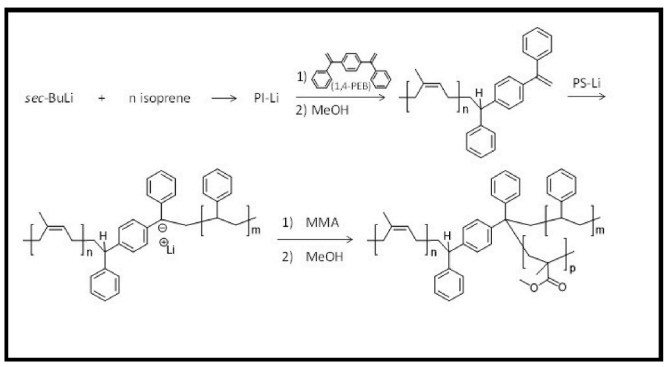

Scheme 1. General polymerization scheme for synthesizing ISM miktoarm star terpolymers.

Table 1
The size and pairwise segregation strength, $\chi_{AB}N_{AB}$, of the ISM miktoarm star melts at 150 °C, where f_i is the volume fraction of component i, $N = \sum_{i=1}^{3} N_i$, and N_{AB} is the combined N for the corresponding AB-diblock copolymer. I: Isoprene, S: Styrene, M: Methyl methacrylate.

	f_{PS}	f_{PI}	f_{PMMA}	N	$\chi_{IS}N_{IS}$	$\chi_{IM}N_{IM}$	$\chi_{SM}N_{SM}$
ISM2.2	0.25	0.24	0.51	810	20	37	11
ISM3.7	0.19	0.18	0.63	1086	20	54	16
ISM5.4	0.14	0.14	0.72	1414	20	74	21

Table 2
Characteristics of the synthesized ISM star block terpolymers and their precursors. Bulk morphology from SAXS.

Name	MW, kDa (NMR)	Đ (GPC)	[a]PI:PS:PM volume ratios (NMR)	[b]Morphology (SAXS)	[c] L_o or d_{10}, nm (SAXS)
PI	9.8	1.05	1 : 0: 0	n/a	n/a
PS	11.7	1.04	0 : 1: 0	n/a	n/a
PI-PS	21.5	1.04	1 : 1: 0	n/a	n/a
ISM2.2	49.3	1.04	1 : 1: 2.2	LAM	27.3
ISM3.7	68.0	1.07	1 : 1: 3.7	HEX	31.4
ISM5.4	90.2	1.10	1 : 1: 5.4	HEX	36.9

[a] Volume ratios (v:v:v) of the blocks were estimated by ^{1}H NMR ($CDCl_3$, 400 MHz) using room temperature densities of poly(1,4-isoprene) [0.91 g/ml], poly (styrene) [1.06 g/ml] and poly(methyl methacrylate) [1.18 g/ml].

[b] Hexagonally packed cylinders (HEX) and lamellar (LAM) morphologies were determined from SAXS relative peak positions.

[c] The characteristic distance, L_0 (LAM) or d_{10} (HEX) is given by $2\pi/q^*$, where q^* is the first order peak position.

assignment of NMR peaks and relative intensities are found in the Supplementary Information (Figs. S9 and S10 and Table S4). The progress of the synthesis and purity of the final stars were followed by GPC as illustrated in Fig. 1.

Sample preparation and thin film preparation for TEM staining by OsO_4 and by RuO_4, respectively, followed Chernyy et al. [41]. Staining times were 4h for OsO_4 and 30 min for RuO_4. TEM was obtained using a FEI Tecnai T20 G at 200 kV accelerating voltage in a bright field mode.

For SAXS, ~0.5–1 mm polymer films were produced by solvent casting from 7% THF solutions under N_2 for 1 week in the dark, followed by thermal annealing for 5 days at 150 °C. SAXS curves were measured at CHESS, Cornell University, USA, at the D1 beamline with a monochromatic 10.6 keV beam (λ = 0.117 nm, monochromatised by Mo/B_4C multilayers). The flux and the energy resolution were 10^{12} photons/(s mm^2) and $\Delta E/E$ = 1.5%, respectively. The sample-to-detector distance was 1750 mm, and the X-ray beam size was 0.5 × 0.2 mm^2 (horizontal × vertical). Scattered radiation from the samples was collected on a PILATUS3 200k (487 × 407 pixels with 0.172 × 0.172 mm size) detector (Dectris Co.) at room temperature. 2D scattering images were reduced to the corresponding transmission corrected and background subtracted 1D SAXS patterns by azimuthal integration (0°–180°) after bad pixel masking and detector/beam stop dead area removal utilizing fit2D [64,65]. The curve fitting toolbox in Matlab is used to fit Gaussian curves to the experimental data and evaluating them [66].

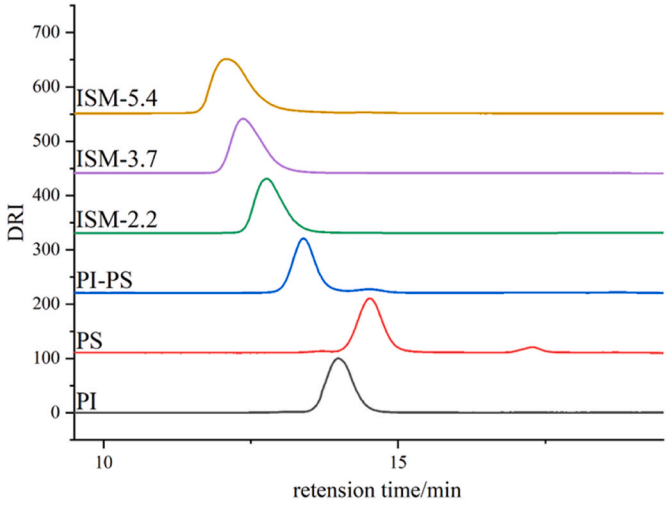

Fig. 1. GPC curves of the synthesized ISM stars and their precursors. Column system: guard column and 8 × 300mm^2 PLGel Mixed-D column. Eluent THF at 0.5 ml/min. DRI detection (differential diffractometer). Calibration with polystyrene standards. Injection volume 0.1 ml.

Thin ISM star films were spin coated onto clean room grade silicon wafers with native SiO_2 oxide (purchased from Topsil Global Wafers, Denmark) without any further wafer surface cleaning from 1% (for SEM) and 3% (for AFM and XRR) toluene solutions. The spin coating parameters were for the 1% solution for SEM, 6000 rpm/s acceleration and 6000 rpm velocity to achieve thicknesses close to the equilibrium domain spacing (d_0) and for the 3% solutions for AFM/XRR, 6000 rpm/s acceleration and 3000 rpm velocity to achieve ~100 nm films. The samples were solvent vapor annealed (SVA) in non-saturated acetone vapor (0.1 ml acetone, fully evaporated in a 200 ml vial) for ~1 day. SEM of the thin films was obtained using a Zeiss Supra 40VP at 1 kV accelerating voltage and 3–5 mm working distance without extra film treatment (i.e. no additional gold/carbon sputtering). The SEM images were recorded at different times before and after equipment renovation, i.e., the contrast of the images cannot be directly compared. AFM was performed using a NX20 (Park Systems Co.) with high-resolution OMCL-AC160TS rectangular cantilevers (force constant = 26 N/m and Resonance Frequency = 300 kHz) in non-contact mode. AFM Root Mean Square (RMS) roughness of the films were obtained from height scans with XEI SPM image processing tool (Park Systems Co.). Fast Fourier Transform (FFT) of the SEM micrographs and the 1 μm × 1 μm AFM height scans along with the corresponding radially integrated plots were calculated using ImageJ software [67]. XRR of thin films was realized on a Rigaku (SmartLab) X-ray Diffractometer equipped with a rotating anode (High voltage = 45 kV, I = 200 mA, beam-height = 50 μm and Cu $K_{\alpha 1}$ radiation with λ = 0.154 nm (Incident Ge 220 double bounce monochromator)) with 2θ = 0–5° with a step size and continuous scan speed of 0.004° and 0.08° min^{-1}, respectively. XRR curve simulation and fitting to experimental data are performed using GenX [68]. As-cast and annealed film thicknesses were measured by optical reflectometry (OR) using a Nano Calc-XR reflectometer with an external (UV-VIS-NIR) light source (all from Ocean Optics Co.) using incident light with a wavelength in the range of 400–850 nm. The thickness of the native oxide layer of the bare wafers was measured using a variable angle spectroscopic ellipsometer (M − 2000, J. A. Woollam Co., Inc.).

The relevant pairwise Flory-Huggins interaction parameters are partially available in the literature. The values given here are intended to put the data presented in qualitative perspective by referring to di-BCP theory, i.e., comparing the ISM star BCP arms pairwise. We are not using the exact χ-values for quantitative analysis. The χ-values and degrees of polymerization, N, are based on a reference volume of 0.1 nm^3 and ρ_{PI} = 0.824 g/cm^3; ρ_{PS} = 0.964 g/cm^3; ρ_{PMMA} = 1.124 g/cm^3 [69]; χ_{IS} = 0.0494 and χ_{SM} = 0.0175 [70] all at 150 °C, which is the temperature used for thermal annealing of bulk samples. χ_{IM} has not been measured. Tcherkasskaya et al. has reported a value for PI-PMMA [71]. However, this value (0.061 when recalculated to the 0.1 nm^3 reference volume) is measured for predominantly 3,4/1,2 addition PI whereas the present sample is predominantly 1,4-PI. Furthermore, the value is based on measurement of the interphase width in block copolymers and assuming the strong segregation theory prediction for the width. In lieu of a better value, we crudely assume the value ~0.061 to be relevant here and thus, implicitly assume that the isoprene addition mode in the chain does not influence the interaction. These

considerations lead to the characteristics of the ISM stars reported in Table 1. Thus, the PS-PI and the PS-PM blocks are weakly segregated (5–10 < χN <29) whereas the PI-PM interaction is in the medium to strong segregation regime at 150 °C (30 < χN<75) [72]. A summary of bulk properties for the three synthesized star blocks, ISM2.2, ISM3.7 and ISM5.4 are found in Table 2.

3. Results and discussion

3.1. Synthesis

The previously published synthesis of ISM stars [59] is based on coupling of living polymer chains employing relatively laborious chlorosilane chemistry. The present synthesis employs a method previously used for other ABC miktoarm stars [41,42]. The general method is outlined in Scheme 1 for ISM stars but will work for 3-arm stars where the first block can be terminated with a DPE functionality, and where the living chain of the next block can react with the DPE functionality to form a DPE lithium based macro initiator. For the third block it is a requirement that the polymerization can be initiated by 1,1-diphenyl alkyl lithium. In the case of ISM stars, the PI-Li was end-capped with 1,4-PEB. Here it is important to notice, that while the two double bonds in 1,4-PEB are equivalent at the outset, once the 1,4-PEB has reacted, the reactivity of the double bond left is substantially reduced. This fact greatly minimizes the probability for coupling reactions in the first step. For the addition of the second arm, advantage is taken of the fact that DPE does not homopolymerize. Unavoidable weakly acidic impurities, that would terminate the second block, are titrated with 1,1-diphenylhexyl lithium without interfering with the macromonomer. For the third block, advantage is taken of the living nature of the reaction which allows for sequential addition of monomers and allows withdrawal of aliquots of the reaction mixture at each step to afford a series of ISM stars with low dispersity, Đ (Đ = M_w/M_n, where M_w is the weight average molecular weight and M_n is the number average molecular weight) and with identical PI and PS arms but with varying molecular weight of the PMMA arm.

3.2. Bulk morphology (SAXS and TEM)

The bulk morphology of the homologous series of three ISM star polymers synthesized and characterized as described above and in Tables 1 and 2, were investigated with SAXS and TEM.

A schematic drawing of relevant structures referred to throughout the paper is seen in Fig. 2.

3.2.1. Small-angle X-ray scattering

The SAXS profiles of the ISM stars as a function of the scattering vector, q, were measured at room temperature after thermal annealing (see Fig. 3). X-ray scattering results from the spatial variations of the electron density due to microphase separation of the three different polymer blocks in the ISM stars. The electron densities for the pure polymer phases are 3.09×10^{23} e/cm^3 for PI, 3.37×10^{23} e/cm^3 for PS, and 3.90×10^{23} e/cm^3 for PMMA calculated based on the room temperature mass densities tabulated in the footnote of Table 2. Assuming nano-sized domains of pure polymers, the SAXS scattered intensity is proportional to the polymer electron contrast squared, i.e. the square of the differences of the electron densities of the three blocks: $(\rho_{e,PS} - \rho_{e,PI})^2 = 0.78 \times 10^{45}$ (e/cm^3)^2, $(\rho_{e,PS} - \rho_{e,PMMA})^2 = 2.81 \times 10^{45}$ (e/cm^3)^2 and $(\rho_{e,PI} - \rho_{e,\ PMMA})^2 = 6.56 \times 10^{45}$ (e/cm^3)^2. Hence, the major contributions to SAXS arises from the electronic contrast between PI and PMMA or between PS and PMMA. The volume fraction of PMMA is dominant in all three ISM stars and this further adds to the difficulty of distinguishing PS-PI microdomains by X-ray scattering. In accordance with the Flory-Huggins parameters (i.e. $\chi_{IM} > \chi_{IS} \gg \chi_{SM}$), and in accordance with earlier experimental results, PS is mediating between sharply separated PMMA and PI blocks [58,62,71]. In addition, since PI is a minority domain in a matrix dominated by PMMA, and the scattering contrast between PI and PS is low, the scattering is mainly determined by the PI microdomain size, shape and spatial configuration. For each sample, the peak position, q^*, of discernible Bragg peaks are located by fitting Gaussian functions to the experimental data in a narrow q-range around each peak. The fitting coefficients are listed in Table S1 in the Supplementary Information [66].

For ISM2.2, a highly ordered lamellar microdomain morphology was observed with a domain spacing, $L_0 = 2\pi/q^* = 27.3$ nm ($q^* = 0.23$ nm^{-1}), as evidenced by the multiple higher order reflections at scattering vector positions 1:2:3 relative to the position of the primary reflection, q^* (Fig. 3). This indicates, consistent with theoretical phase diagrams [41,51], that PMMA and PI/PS arrange in lamellar microdomains for ISM2.2 with PMMA lamellar domains alternating with lamellae consisting of PS and PI. For ISM3.7, three reflections at peak position ratios of $1:\sqrt{3}:\sqrt{7}$ relative to the first-order peak, q^*, can be identified (a $\sqrt{4}$ peak cannot be discerned) and were characterized by the characteristic distance, $d_{10} = 2\pi/q^* = 31.4$ nm ($q^* = 0.20$ nm^{-1}). This indicates that the PI/PS minority domains are arranged in hexagonally packed cylindrical microdomains in a matrix of PMMA [73]. A likely scenario is that PI forms the core of the cylinders with a surrounding shell of PS mediating contact between domains of pure PMMA and pure PI. The center to center rod distance, i.e. the cell edge length, a,

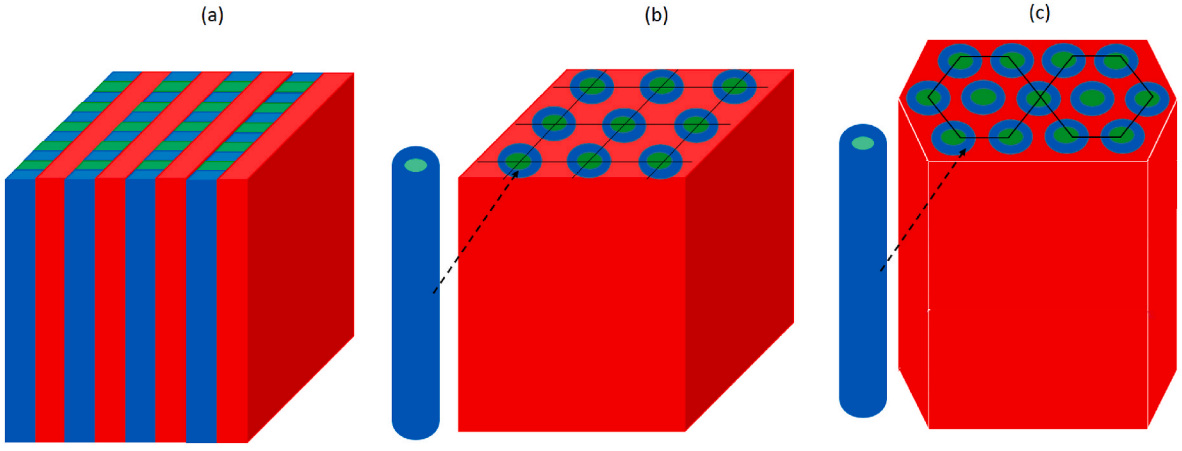

Fig. 2. Schematics of structures found for the three ISM star samples. a) Alternating lamellar structure [ALT.LAM], b) Core-shell cylinders packed on a square lattice (a single core-shell cylinder is also shown), c) Core-shell cylinders packed on a hexagonal lattice (HEX) (a single core-shell cylinder is also shown). Red is corresponding to the PMMA arm, blue to the PS arm and green to the PI arm. (For interpretation of the references to color in this figure legend, the reader is referred to the Web version of this article.)

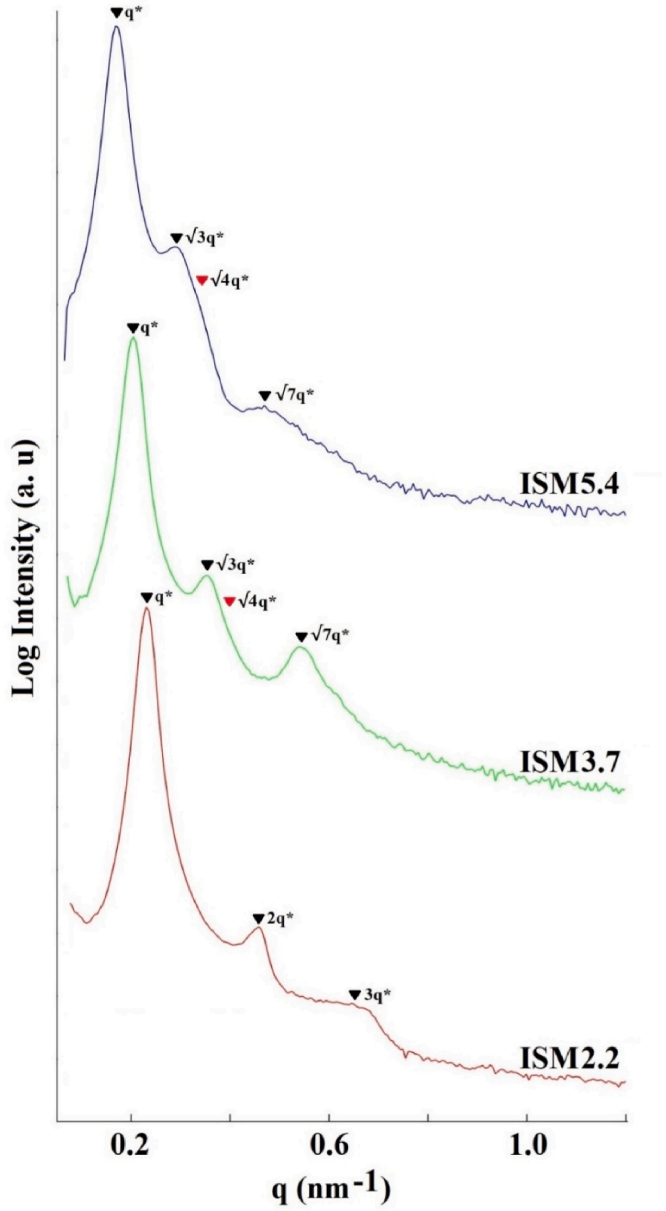

Fig. 3. SAXS intensity profiles (measured at room temperature) as a function of scattering vector q for ISM miktoarm star terpolymers thermally annealed at 150 °C under vacuum for 5 days. Relative positions of Bragg peaks are marked. The $\sqrt{4}$ q* reflections marked with a red arrow cannot be discerned. Intensity profiles are scaled for clarity.

of the ISM3.7 structure is given by $a = 2d_{10}/\sqrt{3} = 36.3$ nm [73]. The sample with the largest volume ratio of PMMA, ISM5.4, have less pronounced Bragg peaks at positions also corresponding to hexagonal packing of rods with relative peak positions $1:\sqrt{3}:\sqrt{7}$ (also here no $\sqrt{4}$ peak can be discerned) with $d_{10} = 2\pi/q^* = 36.9$ nm ($q^* = 0.17$ nm^{-1}), giving a center to center rod distance, a, of 42.6 nm. The transition from lamellar to hexagonal structure is driven by the increasing volume fraction of PMMA consistent with theoretical calculations and other experimental observations of comparable systems [41]. Peak intensities (see Table S1, specifically 3rd order peaks) diminish with increasing PMMA block length in ISMs with hexagonal symmetry. The bulk morphologies obtained are supported by TEM as shown below. The lack of discernible $\sqrt{4}$ reflections is probably related to interference effects from the presence of three polymer domains (the analysis above is pseudo two domain). The structures obtained for the star architecture are similar to the morphologies found for linear ISM tri-BCPs [74,75], where ordering was induced in ISM melts by blending with PI, PS and PMMA homopolymers, respectively.

3.2.2. Transmission electron microscopy

From the SAXS data, it was not possible to determine the detailed morphology of the PI/PS microdomains, hence, bright field TEM of the ISM star samples complements the SAXS data as shown in Fig. 4. For morphological analysis of the bulk samples, TEM was performed using two different staining agents, RuO_4 and OsO_4. OsO_4 preferentially stains the PI phase, which then appears dark, whereas the PS and PMMA phases are less distinguishable and appear as light areas. RuO_4 leaves PMMA unstained, i.e., in this case, PMMA appear lightest [57–59]. The micrographs in Fig. 4 overall confirm the result from SAXS, i.e., the bulk morphology is the same for ISM3.7 and ISM5.4, while ISM2.2 has a bulk morphology distinct from the two higher PMMA volume fraction samples. In particular, it is seen from the top row RuO_4 stained micrographs, that the structure has lamellar periodicity for ISM2.2, i.e., alternating rows of light (unstained PMMA) and dark (indistinguishable PI and/or PS) stripes are seen. When staining ISM2.2 with OsO_4 (bottom row in Fig. 4), in every second stripe appearing dark (PI), lighter areas across the stripe indicate the presence of PS (assuming PI and PMMA avoid contact) similar to what is observed in Refs. [74,75]. The light elongated areas are consistent with PMMA lamellae adjacent to the PS/PI lamellae. This structure of alternating lamellae is denoted [ALT.LAM] [41]. The [ALT.LAM] morphology has also been observed in other ABC miktoarm star systems composed of polydimethylsiloxane, PI, and PMMA or PI, PS, and Poly(2-vinylpyridine) [24,41,42].

The first row micrographs in Fig. 4 from ISM3.7 and ISM5.4, reveal in both cases a honeycomb structure with hexagonally packed columns/cylinders of undistinguishable PI/PS (i.e. dark stained blocks) embedded in a PMMA (i.e. the light unstained block) matrix. While PS is indistinguishable from PI on the top row images (dark areas), PS is indistinguishable from PMMA on the bottom row images (light areas). This is consistent with PS forming a shell around the PI cylinder core domains. This interpretation is consistent both with the SAXS images and with the relative values of the pairwise Flory-Huggins interaction parameters, i.e. PS is located between the PI and PMMA blocks in order to decrease the non-favorable contacts between these domains.

The core-shell structure has been observed previously in linear ISM tri-BCPs [74–76]. Similar behavior was also observed in star BCPs composed of PI, PS, and poly(2-vinylpyridine) (P2VP), where the non-favorable PI/P2VP contact was minimized by intervening PS layers and in star BCPs composed of PI, PMMA and poly(dimethyl siloxane) (PDMS), where PDMS domains are placed to prevent non-favorable PI/PMMA contacts [41,42].

The broad domain boundaries between the weakly segregated PS and PMMA blocks in the quasi bi-domain TEM micrographs confirms a certain degree of partial mixing. Previous work on the bulk structure of ISM stars covering other ranges of block pair χN, also identified columnar PI regions surrounded by a shell of PS in a matrix of PMMA [57–59] and hexagonal packing of columns was also observed. However, no [ALT.LAM] structure and no square lattice packing (see below) was observed for these bulk ISM systems.

Thus for the bulk structure of the homologous series of ISM star BCPs at room temperature after annealing at 150 °C, SAXS and TEM results are consistent with a structure of PS/PI and PMMA alternating lamellae for the sample with PI:PS:PMMA volume fraction equal to 1:1:2.2 changing to a core-shell cylinder structure with PI constituting the cylinder core surrounded by a PS shell and hexagonally packed in the PMMA matrix for PI:PS:PMMA volume fractions equal to 1:1:3.7 and 1:1:5.4. This is consistent with both theory and experiments on similar systems when the arm length of one block is increased while keeping the length of the other two fixed [41,42,51].

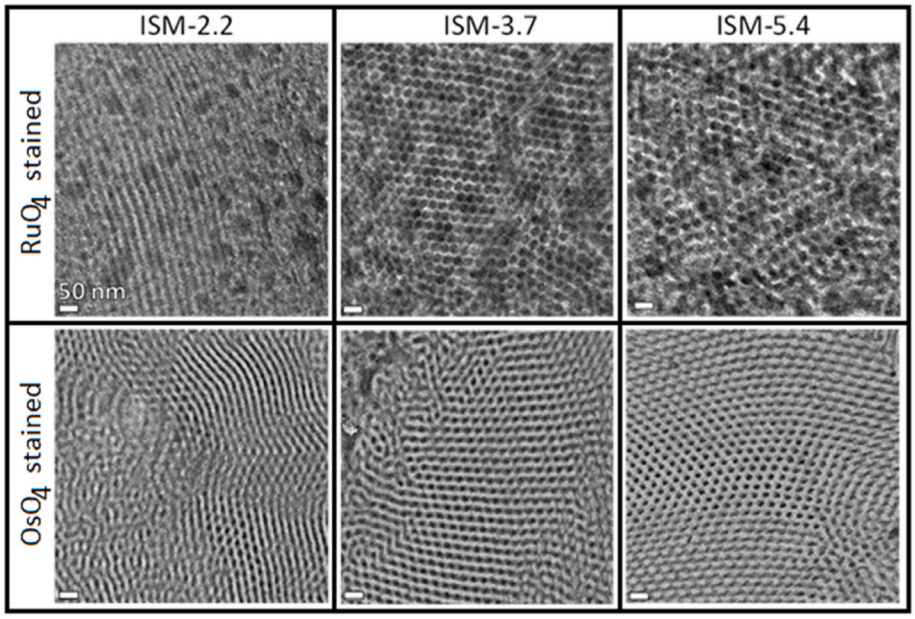

Fig. 4. TEM images (taken at room temperature) of RuO_4 stained (top row) and OsO_4 stained (bottom row) ISM star samples after thermal annealing at 150 °C for ~5 days.

3.3. Thin film morphology (SEM, AFM and XRR)

It is well established that block copolymer thin film morphology might differ from the bulk morphology of the same system since additional interactions between the constituent blocks and the substrate (e.g. silica) and/or the free surface (air) might affect the morphological behavior of the system in the thin films. In addition, lack of commensurability between the characteristic morphological length scale and the

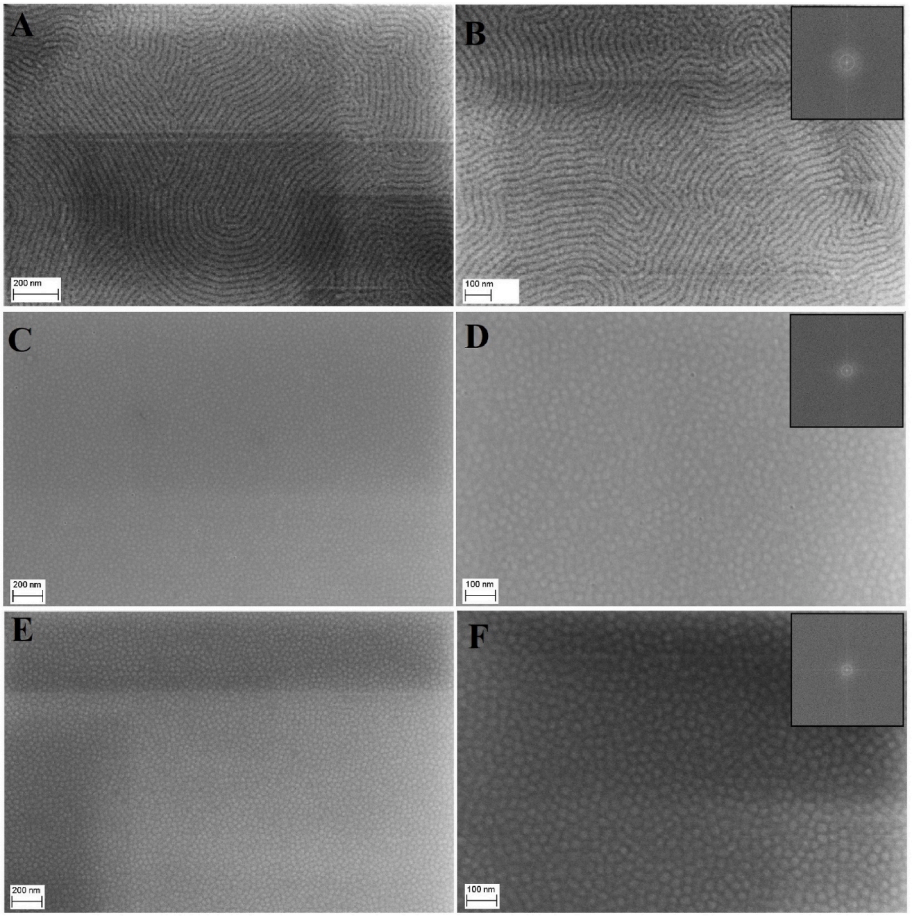

Fig. 5. SEM images of the thin films of ISM2.2 (A, B), ISM3.7 (C, D) and ISM5.4 (E, F) after SVA (in 0.1 ml acetone vapor in 200 mL capped container for ~1 day), lower magnification (A, C, E) and higher magnification with the corresponding 2D-FFT patterns as insets (B, D, and F).

film thickness can influence the morphology [41,77,78]. The PI arm has the lowest surface tension of the three blocks in the ISM stars ($\gamma_{PI} = 31$ mN/m [41]; $\gamma_{PMMA} = 41$ mN/m [41] and $\gamma_{PS} = 33$ mN/m [79]) and accordingly tends to preferentially segregate to the polymer/air interface [77]. PMMA is the most polar arm of the three blocks, but only slightly more so than PS. Earlier studies have shown that for PS-PMMA, PMMA will be prone to form a layer next to the substrate SiO_2, while PS will form a layer at the air-polymer interface [80]. At room temperature, the PI domain with glass transition temperature, $T_g \approx -65$ °C is in the rubber state, while the PS and the PMMA blocks are in the glassy state with $T_g \approx 100$ °C and $T_g \approx 105$ °C, respectively [57–59], which will influence the ability to form wetting layers at the interfaces [74]. In addition, the ABC junction points in miktoarm stars are confined to a line, giving less freedom in restructuring than for linear BCPs [55,56,81], which might make the formation of wetting layers difficult for star architecture.

Hence, to address possible differences between bulk and thin film morphology, studies of ~ 30 nm (comparable to the microdomain length scale) and ~ 100 nm (corresponding to few microdomains) thin ISM star films are performed using SEM and AFM for surface morphology. XRR studies are performed primarily to illuminate the possibility of wetting layers formed at the film interfaces.

3.3.1. Scanning electron microscopy

For SEM studies, the thickness of the films (~ 30 nm) was chosen close to the equilibrium domain spacing values ($d_0 = 27$–37 nm), hence the film is about two star-molecules thick. The contrast is based on the natural contrast between the materials with no additional metal sputtered on the surface. The SEM is run at a very low accelerating voltage, and PMMA is expected to appear gray, while PI appears dark [41]. As is seen in the SEM micrographs (Fig. 5), the morphology for ISM2.2 is alternate lamellae [ALT.LAM] seen as light PMMA stripes and darker stripes with alternating PS and PI domains. The overall behavior is consistent with the bulk TEM images. However, contrary to the TEM images, which displayed relatively vague structures, on the SEM images, the alternate structure with one lamellae of a single polymer block and a lamellae with alternating regions of two different polymer blocks inside the lamellae, is clearly identified. Micrographs of ISM3.7 and ISM5.4 show a bi-domain morphology – three phases cannot be clearly distinguished in contrast to the ISM2.2 case. ISM3.7 and ISM5.4 thin films shows light areas enclosed in a darker matrix. This is interpreted as a rod-like structuring perpendicular to the substrate. The colors cannot be directly compared with the micrograph for ISM2.2 due to instrument refurbishing, however the light color of the enclosed domains relative to the matrix, might indicate a more profound mixing of PI and PS than found for ISM2.2. The rods appear relatively irregularly packed and irregularly shaped in contrast to what was found for the bulk systems, possibly due to fast solvent removal from the very thin film after solvent vapor annealing. It is also probable that surface interactions cause deviations from the bulk structure. The reduced chain mobility in glassy spin-coated films may account for the inability of the star BCPs to form well-defined and well-ordered tri-domain surface morphologies, at least for longer arm lengths. Another possibility for not observing three distinct domains in SEM images of ISM3.7 and ISM5.4 could be due to the weakly segregated PS and PMMA blocks, i.e., these blocks may also be partially mixed, PS thus forming a zone between PI and PMMA with a relatively large degree of intermixing. The combination of low electron density contrast between PS and PI and their low volume fractions in ISM3.7 and ISM5.4 can also make distinguishing between the PI and PS blocks difficult. The inserts in Fig. 5 b, d, e show Fast Fourier Transform (FFT) of the SEM images. For ISM2.2 two rings are observed with relative positions 1:2, confirming the 2D powder-like lamellar order. For ISM3.7 and ISM5.4, a single ring is observed indicating a typical nearest neighbor distance. For thin films, it is concluded, as was found for bulk systems, that the ISM2.2 morphology is different from the systems with larger PMMA arm length ratios. In contrast, the structure for ISM3.7 and ISM5.7 is similar to each other but distinct from the bulk behavior, since the encapsulated domains appear more disordered and less well-defined in shape.

3.3.2. Atomic force microscopy

Fig. 6 shows AFM height scans (non-contact mode) of acetone annealed ~100 nm thick ISM star films. All three annealed ISM samples show ordered structures, while the corresponding as-cast ~100 nm thick films show no longer range order (see Fig. S1 in supplementary information). This suggests acetone is a good choice for solvent vapor annealing of the ISM films as also judged from the value of the Hildebrand solubility parameters (see below).

The AFM images seen in Fig. 6 generally appear with two clearly distinguishable domains. For annealed samples, height differences between glassy (PS and PMMA) and rubbery (PI) blocks is expected to occur due to differences in mobility during drying after annealing, i.e., PI domains are generally lower in height than PS and PMMA domains, while AFM height scans cannot distinguish between the two glassy blocks. From AFM (thin film surface structure), the same picture emerges as was observed using SAXS for the bulk structure: the lowest PMMA arm ratio sample has a structure distinctly different from the two longer PMMA arm length ratio samples. All data, both for bulk samples and for thin films are consistent with ISM2.2 having a lamellar structure with PMMA forming one set of lamellae and PI and PS forming another set of lamellae with an internal patterning of the lamellae with alternating PI and PS domains. As seen from Fig. 6, the symmetry for annealed ISM3.7 and ISM5.4 is distinctly different from ISM2.2: dark round(ish) areas (holes) are enclosed in the lighter colored protruding matrix. This is consistent with a standing cylinder structure as also indicated by SAXS and TEM. There is no trace of a wetting layer in the annealed films at the polymer/air interface, consistent with both PI (with the lowest surface tension) being a strongly segregated minority component and with the restricted flexibility enforced by the location of ABC star junction points on a line. Overall, the different film structures are similar to the SEM results obtained from the very thin films described above, however there are important differences. While the dark areas for the thicker ISM3.7 film are packed in a hexagonal pattern (with a large degree of disorder), the dark areas are packed on a square lattice with a relatively high degree of order for the thick film longest PMMA arm sample, ISM5.4. The room temperature Young's moduli of PI, PS and PMMA is 1–2 MPA, 3 GPa and 4.8 GPa, respectively [82–84] with PI having a T_g well below RT, while T_g for PS and PMMA are well above RT. During solvent vapor annealing, the T_g for the different blocks are lowered and when drying, PS and PMMA enters the glassy state again at some point, while PI stays rubbery. Hence, PS and PMMA are prone to making protrusions during drying, while the PI block continues to be flexible enough for chain rearrangements to occur. Accordingly, PI domains appears dark, i.e. have lower relative heights in the AFM height scans. Comparing the Hildebrand solubility parameter, δ, of the ISM blocks in the annealing solvent vapor, acetone is a better solvent for the PMMA block ($\delta_{acetone} - \delta_{PMMA} = 0.9$) than for the PS ($\delta_{acetone} - \delta_{PS} = 1.4$) and the PI ($\delta_{acetone} - \delta_{PI} = 3.4$) blocks [77]. The packing of ISM5.4 changes from hexagonal in bulk (TEM) to square lattice in the ~100 nm thick (corresponding to about six molecular layers) film and to irregular packing of domains in the PMMA matrix for the ~30 nm thick film. The change from hexagonal packing to square lattice packing is somewhat similar to the findings in Ref. [85], where binary blends of (poly(isoprene-*b*-styrene-*b*-(2-vinylpyridine)) thin films exhibit hexagonal and tetragonal patterns depending on annealing time. Calculations of the equilibrium free energy of lamellar, cylindrical, and spherical structures for linear ABC block copolymers in which A and C blocks are of similar volume fractions and form separate minority domains dispersed in matrix B, show that for low combined volume fractions of the A and C blocks, cylinders on a square lattice become the most stable packing [86]. In the present case, the different packing of rods for bulk and in ~100 nm films are probably linked to surface energy contributions.

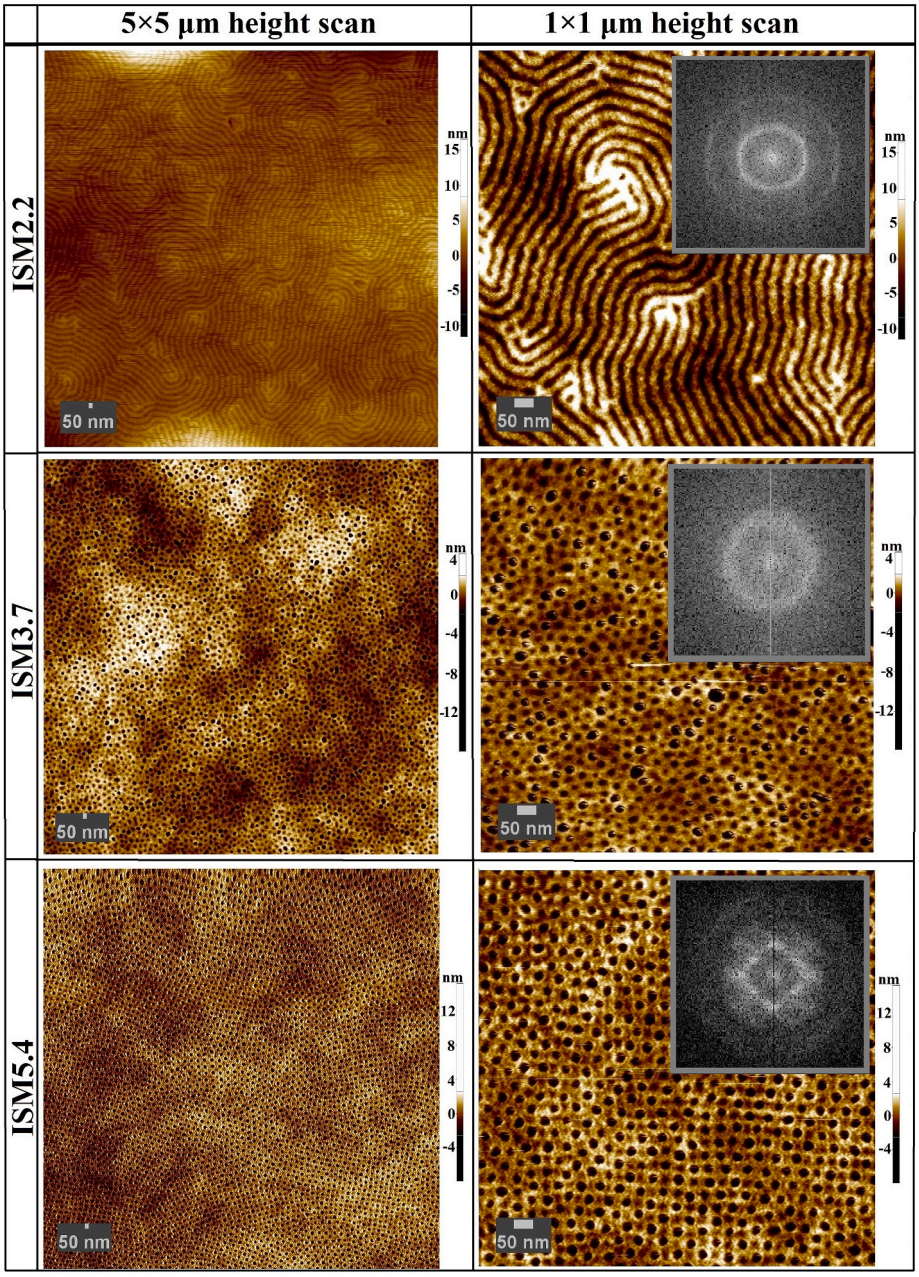

Fig. 6. AFM height scan micrographs of ~100 nm thick films of ISM2.2, ISM3.7 and ISM5.4 on Si-wafers. The images are from solvent vapor annealed films (in 0.1 ml acetone vapor in 200 mL capped container for ~1 day). The first column shows 5 μm × 5 μm height scans and the second column shows 1 μm × 1 μm height scans with the corresponding 2D-FFT patterns as insets.

Incommensurability of the film thickness with the domain spacing probably plays a role for the different morphologies of ~30 and ~100 nm thick films.

The quality of ordering in the top layer of the thin films were analyzed by performing Fast Fourier Transform (FFT) on the 1 μm × 1 μm AFM height scans (see the insets in Fig. 6). Utilizing ImageJ software [67], the intensity of the 2D-FFT patterns are summed radially for a quantitative evaluation (see Fig. S2 and Table S2). The radial integration profiles show relative q^* peak positions 1:2 for ISM2.2 and $1:\sqrt{2}:\sqrt{5}$ for ISM5.4. This result suggests a lamellar structure for the former and a square lattice structure for the latter [87]. The ISM3.7 film has PI rods distributed on a highly irregularly hexagonal lattice in the PMMA matrix. Hence, no higher order peak(s) are discerned in the radial integration profile of ISM3.7. Similar to the bulk SAXS analysis, the position of the first order peak was used to calculate the surface domain spacing (d_{s0}) of the samples (see Table 3). We note that the d_{s0} values are larger than the corresponding bulk values, L_o or d_0, obtained from SAXS measurements (see Table 3). We attribute this difference to surface energy contributions in the thin films, and a possible incommensurability between the total film thickness and the domain spacing, which can lead the blocks to stretch or contract in thin films [41]. The differences may also arise from the resolution limitations of the AFM tip.

3.3.3. *X-ray reflectometry*

According to AFM, the thin-film star samples have no wetting layers present at the polymer/air interface. However, in order to investigate the interior of the film, i.e., to decide whether a wetting layer is formed at the film/substrate interface, and to assess any layering inside the film, we employed XRR analysis of the as-prepared spin-coated ~100 nm thick films and the corresponding acetone annealed samples. The

Table 3
Comparison of SAXS (bulk L_o or d_0 – see Table 2) and AFM FFT (thin film d_{s0}) peak locations and corresponding domain spacing. See also Table S1 and S2 together with Fig. S2 in the Supplementary Information.

Sample	Peak	bulk (nm^{-1})	thin film (nm^{-1})	[a]L_0 or d_0 in bulk (nm)	[b]d_{s0} in film (nm)
ISM2.2	q*	0.23	0.18	27.3	34.9
	2q*	0.46	0.36		
	3q*	0.69	n/a		
	4q*	0.92	n/a		
ISM3.7	q*	0.20	0.17	31.4	37.0
	√3q*	0.35	n/a		
	√7q*	0.54	n/a		
ISM5.4	q*	0.17	0.16	36.9	39.3
	√2q*	–	0.24		
	√3q*	0.29	–		
	√5q*	–	0.35		
	√7q*	0.45	–		

[a] Obtained with SAXS.
[b] Obtained with AFM.

experimental XRR profiles of the films (Fig. 7) were simulated using the GenX program package [68] and a model with a number of horizontally stacked layers consisting of ISM stars together with potential wetting layers at the two interfaces; the substrate and the native SiO_2 layer on top of the substrate. It is important to note, that XRR cannot resolve any lateral structure, i.e. the electron density is averaged in the plane perpendicular to the film normal. We assume that the polymer layer consists of basic units (i.e. single star molecules) with known composition, density, and X-ray Scattering Length Density (SLD), which is listed in Table S3 in the Supplementary Information. We model ISM2.2, ISM3.7 and ISM5.4 as layers with an average composition corresponding to the respective constituent blocks and volume fractions. The simulated XRR profile for each layered system is fitted to the experimental data using GenX [68]. The layered systems consist of at least 3 (i.e. Si substrate + native SiO_2 oxide + ISM stars) to at most 5 layers (i.e. Si substrate + native SiO_2 oxide + possible polymer/substrate wetting layer + ISM stars + possible polymer/air wetting layer) stacked on top of each other. To decrease the large number of fitting parameters, we have measured a bare Si-wafer (Fig. S3 in Supplementary Information) to obtain the thickness, density and roughness of the native oxide layer, together with the substrate density. The XRR profile of the bare Si-wafer is also measured in order to specify instrumental parameters (e.g. incoming X-ray intensity, illuminated sample length etc.). The XRR fit results yielded a SiO_2 layer thickness of 1.4 nm and a RMS roughness of 0.4 nm for the bare wafer, which were verified with OFTM (optical reflectometry) (Fig. S4), ellipsometry (Fig. S5) and AFM height scan (Fig. S6). The fitting process of the simulated XRR profiles to the experimental XRR data of the ISM star films were performed under fixed instrumental, oxide and substrate parameters. The best fits to the experimental data were obtained with an ISM star layer on top of the Si-wafer with a native SiO_2 layer (Fig. 7). The results (see Table 4, Table S3 and Fig. S8), did not suggest the existence of any wetting layers on the polymer/substrate or the polymer/air interface, possibly due to limitations in the movements of the junction points in the star polymers [58]. The amplitude of the Kiessig fringes increases from ISM2.2 to ISM5.4. This is due to the larger PMMA content (with higher electron density than PI and PS) for ISM5.4 than ISM3.7 and ISM2.2. The fringes die out faster for all the annealed films, which can be explained by rougher film surfaces after annealing. This may be due to creation of protrusions during drying [88]. The film thickness is increased 2–3% after drying (see Table 4 and Figs. S7 and S8) probably due to residual solvent in the film after SVA [89]. This is probably because of the affinity of acetone to PMMA [77].

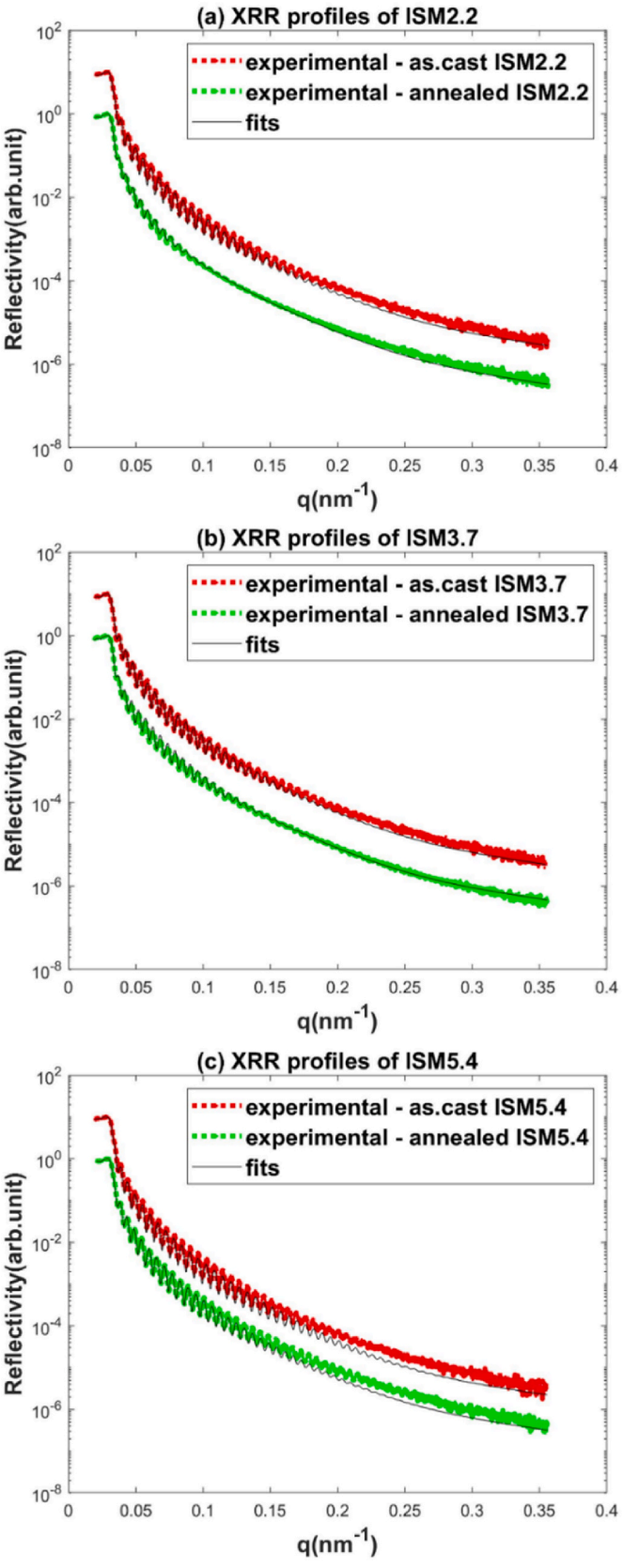

Fig. 7. Experimental XRR profiles and the corresponding best fits (see text) for 100 nm ISM2.2, ISM3.7 and ISM5.4 thin films on a Si-wafer (with 1.4 nm native Silicon oxide) before and after annealing (in 0.1 ml acetone vapor in 200 mL capped container for ~1 day). XRR profiles are scaled by a factor of 10 for clarity.

Table 4
Comparing the fitted thickness and root mean square (RMS) roughness obtained from the fits to the XRR profiles of the ISM thin films with the corresponding experimental data obtained by Optical Film Thickness Measurement (OFTM), ellipsometry and AFM RMS roughness.

Material	Treatment history	[a]XRR thickness (nm)	[b]OFTM thickness (nm)	[d]XRR RMS roughness (nm)	[e]AFM RMS roughness (nm)
ISM2.2	As.cast	99.2	100.7	1.3	1.0
	SVA	103.9	102.9	2.5	2.0
ISM3.7	As.cast	104.3	104.2	1.4	0.9
	SVA	107.5	107.3	1.7	1.0
ISM5.4	As.cast	100.6	99.2	1.1	0.9
	SVA	102.4	102.7	1.3	1.3
SiO2	n/a	1.4	1.8(1.78[c])	0.4	0.2
Si	n/a	infinite	infinite	ideally smooth	ideally smooth

[a] The thickness is obtained from the fit to XRR profile with GenX.
[b] The thickness is obtained from a Cauchy fit to white light ($\lambda = 400$–850 nm) reflectance spectrum.
[c] The thickness is obtained utilizing an ellipsometer (M − 2000, J. A. Woollam Co., Inc.).
[d] The roughness is obtained from the fits to the experimental XRR profile with GenX.
[e] The roughness is obtained by AFM analysis of the film surfaces.

4. Conclusion

A homologous series of three low-dispersity ABC miktoarm star terpolymers consisting of PI, PS, and PMMA with systematic variation of the PMMA arm length, were synthesized successfully by living anionic polymerization with a coupling scheme not previously used for synthesis of this system. Also, in contrast to earlier work on similar bulk samples, the present series consist of both weakly segregated and strongly segregated arm pairs. The self-assembled bulk and thin film structures of the star series were investigated with different X-ray and microscopy techniques.

SAXS and TEM were applied for morphological studies of thermally annealed bulk ISM stars. The thin film morphologies of acetone solvent vapor annealed ISM stars were investigated using XRR, AFM and SEM. The ISM star with the shortest PMMA arm length (ISM2.2), exhibit an alternating lamellar structure both in bulk and in thin films consisting of PMMA lamellae and lamellae with alternating PI and PS domains (possibly with some mixing of PS and PMMA). The ISM star with the longest PMMA block length (ISM5.4), in contrast, has in bulk a hexagonally packed structure, consistent with core-shell cylinders (i.e. PI as core and PS as shell) in a PMMA matrix, where the PS shell screens the unfavorable interaction between PI and PMMA. The hexagonal packing of the cylinders change to a square packing in the ~100 nm thick ISM5.4 films, and irregular arrays of standing 'rods' (few molecules) in the ~30 nm thick film. ISM3.7 exhibit hexagonally packed core-shell cylinders in bulk and irregularly packed arrays of standing rods with a trend towards hexagonal packing in thin films with ~100 nm thickness, while in ~30 nm thick films the 'rods' (few molecules) are just as irregularly packed as for ISM5.4.

For the ISM stars in the present work, no wetting layers were formed neither at the air/polymer surface or the polymer/substrate interface for as-prepared or for annealed films, probably due to geometric constraints from the location of junction points on a line. For 100 nm films, the AFM surface patterns show long-range order for the samples with the shortest and the longest PMMA arms, while the irregular arrays of rods in ISM3.7 implies that this sample is in a crossover regime between hexagonal and square lattice packing and accordingly shows only short-range order. An interesting observation is the lack of wetting layers at ISM star thin film interfaces contrary to expected [80]. It thus appears that for the particular choice of polymers forming the star system investigated in this paper, the driving force for forming wetting layers is small enough that packing constraints imposed by the star architecture prevents the formation.

ABC miktoarm star terpolymers are a new class of block copolymer systems, where the molecular architecture plays an important role for nano structuring of corresponding melts. The ISM star system investigated in this paper show core-shell cylindrical structures remaining vertically aligned to the substrate for thicknesses up to several molecular sizes with no wetting layers formed. This point toward ISM stars as having a large potential in nano patterning applications.

CRediT authorship contribution statement

Sina Ariaee: Investigation, Formal analysis, Writing – original draft, Visualization. **Bo Jakobsen:** Software, Data curation. **Poul Norby:** Resources. **Detlef-M. Smilgies:** Resources. **Kristoffer Almdal:** Investigation, Formal analysis, Resources, Writing – review & editing. **Dorthe Posselt:** Conceptualization, Investigation, Formal analysis, Writing – review & editing, Supervision, Project administration, Funding acquisition.

Declaration of competing interest

The authors declare that they have no known competing financial interests or personal relationships that could have appeared to influence the work reported in this paper.

Data availability

Data will be made available on request.

Acknowledgements

Support by the Independent Research Fond Denmark, Project DFF – 7014-00288 (filmSTAR) to D.P. and S.A. is gratefully acknowledged. D. P. and B.J. thank DanScatt for travel support. CHESS is supported by the National Science Foundation through award DMR-1332208. The authors would like to thank the Sergey Chernyy for his contribution to the sample synthesis and for his help with the TEM and SEM measurements. Esben Thorman, DTU is thanked for help and access to perform ellipsometry measurements.

Appendix A. Supplementary data

Supplementary data to this article can be found online at https://doi.org/10.1016/j.polymer.2023.126202.

References

[1] J.N.L. Albert, T.H. Epps, Self-assembly of block copolymer thin films, Mater. Today 13 (6) (2010) 24–33.
[2] H.-C. Kim, S.-M. Park, W.D. Hinsberg, Block copolymer based nanostructures: materials, processes, and applications to electronics, Chem. Rev. 110 (1) (2010) 146–177.
[3] J.A. Liddle, G.M. Gallatin, Nanomanufacturing: a perspective, ACS Nano 10 (3) (2016) 2995–3014.
[4] J. Li, Y. Tu, H. Lu, X. Li, X. Yang, Y. Tu, Rapid synthesis of sustainable poly (ethylene 2,5-furandicarboxylate)-block-poly(tetramethylene oxide) multiblock copolymers with tailor-made properties via a cascade polymerization route, Polymer 237 (2021), 124313.
[5] J. Bang, U. Jeong, D.Y. Ryu, T.P. Russell, C.J. Hawker, Block copolymer nanolithography: translation of molecular level control to nanoscale patterns, Adv. Mater. 21 (47) (2009) 4769–4792.
[6] C.J. Hawker, T.P. Russell, Block copolymer lithography: merging "bottom-up" with "top-down" processes, MRS Bull. 30 (12) (2011) 952–966.
[7] S.-J. Jeong, J.Y. Kim, B.H. Kim, H.-S. Moon, S.O. Kim, Directed self-assembly of block copolymers for next generation nanolithography, Mater. Today 16 (12) (2013) 468–476.
[8] C. Barner-Kowollik, A.S. Goldmann, F.H. Schacher, Polymer interfaces: synthetic strategies enabling functionality, adaptivity, and spatial control, Macromolecules 49 (14) (2016) 5001–5016.

[9] C.M. Bates, M.J. Maher, D.W. Janes, C.J. Ellison, C.G. Willson, Block copolymer lithography, Macromolecules 47 (1) (2014) 2–12.
[10] I.W. Hamley, Ordering in thin films of block copolymers: fundamentals to potential applications, Prog. Polym. Sci. 34 (11) (2009) 1161–1210.
[11] A.P. Lane, M.J. Maher, C.G. Willson, C.J. Ellison, Photopatterning of block copolymer thin films, ACS Macro Lett. 5 (4) (2016) 460–465.
[12] M. Li, C.K. Ober, Block copolymer patterns and templates, Mater. Today 9 (9) (2006) 30–39.
[13] Y. Luo, D. Montarnal, S. Kim, W. Shi, K.P. Barteau, C.W. Pester, P.D. Hustad, M. D. Christianson, G.H. Fredrickson, E.J. Kramer, C.J. Hawker, Poly (dimethylsiloxane-b-methyl methacrylate): a promising candidate for sub-10 nm patterning, Macromolecules 48 (11) (2015) 3422–3430.
[14] K. Koo, H. Ahn, S.-W. Kim, D.Y. Ryu, T.P. Russell, Directed self-assembly of block copolymers in the extreme: guiding microdomains from the small to the large, Soft Matter 9 (38) (2013) 9059–9071.
[15] M.-S. She, T.-Y. Lo, H.-Y. Hsueh, R.-M. Ho, Nanostructured thin films of degradable block copolymers and their applications, NPG Asia Mater. 5 (3) (2013) 42.
[16] A. Aynard, L. Pessoni, L. Billon, Directed self-assembly in "breath figure" templating of block copolymers followed by soft hydrolysis-condensation: one step towards synthetic bio-inspired silica diatoms exoskeleton, Polymer 210 (2020), 123047.
[17] Z. Wang, T. Li, L. Schulte, K. Almdal, S. Ndoni, Photocatalytic nanostructuring of graphene guided by block copolymer self-assembly, ACS Appl. Mater. Interfaces 8 (13) (2016) 8329–8334.
[18] W.A. Phillip, B. O'Neill, M. Rodwogin, M.A. Hillmyer, E.L. Cussler, Self-assembled block copolymer thin films as water filtration membranes, ACS Appl. Mater. Interfaces 2 (3) (2010) 847–853.
[19] G. Dorenbos, Coarse-grained study of the effect of hydrophobic side chain length on cluster size distributions and water diffusion in (amphiphilic-hydrophobic) multi-block co-polymer membranes, Polymer 173 (2019) 43–57.
[20] M. Lee, S. Paria, S. Mondal, G.-B. Lee, B. Shin, S. Kim, S. Park, C. Nah, Amphiphilic block co-polymer and silica reinforced epoxy composite with excellent toughness and delamination resistance for durable electronic packaging application, Polymer 245 (2022), 124679.
[21] J. Wang, Y. Lu, Y. Chen, Fabrication of 2D surface-functional polymer platelets via crystallization-driven self-assembly of poly(ε-caprolactone)-contained block copolymers, Polymer 160 (2019) 196–203.
[22] Q. Zhang, A. Cirpan, T.P. Russell, T. Emrick, Donor–Acceptor poly(thiophene-block-perylene diimide) copolymers: synthesis and solar cell fabrication, Macromolecules 42 (4) (2009) 1079–1082.
[23] N. Hadjichristidis, M. Pitsikalis, H. Iatrou, Synthesis of block copolymers, in: V. Abetz (Ed.), Block Copolymers I, Springer Berlin Heidelberg, Berlin, Heidelberg, 2005, pp. 1–124.
[24] H. Kim, M.M.L. Arras, J.P. Mahalik, W. Wang, D.M. Yu, S. Chernyy, M. Goswami, R. Kumar, B.G. Sumpter, K. Hong, G.S. Smith, T.P. Russell, Studies on the 3-lamellar morphology of miktoarm terpolymers, Macromolecules 51 (19) (2018) 7491–7499.
[25] H. Feng, X. Lu, W. Wang, N.-G. Kang, J.W. Mays, Block copolymers: synthesis, self-assembly, and applications, Polymers 9 (10) (2017).
[26] H. Nikos, H. Iatrou, M. Pitsikalis, S. Pispas, A. Avgeropoulos, Linear and non-linear triblock terpolymers. Synthesis, self-assembly in selective solvents and in bulk, Progress in Polymer Science - Prog. Polym. Sci. 30 (2005) 725–782.
[27] M. Pitsikalis, S. Pispas, J.W. Mays, N. Hadjichristidis, Nonlinear Block Copolymer Architectures, Springer, Berlin, 1998, pp. 1–137.
[28] H.Z. Teruo Fujimoto, Takeo Kazama, Yoshinobu Isono, Preparation and characterization of novel star-shaped copolymers having three different branches, polymer 33 (10) (1992) 6.
[29] Y. Matsushita, K. Hayashida, T. Dotera, A. Takano, Kaleidoscopic morphologies from ABC star-shaped terpolymers, J. Phys. Condens. Matter Institut. Phys. J. 23 (2011), 284111.
[30] H.H. Shigeru Okamoto, Takeji Hashimotot, Teruo Fujimoto, Hongmin Zhang, Takeo Kazama, Atsushi Takano, Yoshinobu Isono, Morphology of model three-component three-arm star-shaped copolymers, polymer 38 (21) (1997) 7.
[31] C.-I. Huang, H.-K. Fang, C.-H. Lin, Morphological transition behavior of ABC star copolymers by varying the interaction parameters, Phys. Rev. 77 (3) (2008), 031804.
[32] K. Jiang, J. Zhang, Q. Liang, Self-assembly of asymmetrically interacting ABC star triblock copolymer melts, J. Phys. Chem. B 119 (45) (2015) 14551–14562.
[33] J.J.K. Kirkensgaard, Striped networks and other hierarchical structures in ${A}_{m}{B}_{m}{C}_{n}$ ($2m+n$)-miktoarm star terpolymer melts, Phys. Rev. 85 (3) (2012), 031802.
[34] J.J.K. Kirkensgaard, M.C. Pedersen, S.T. Hyde, Tiling patterns from ABC star molecules: 3-colored foams? Soft Matter 10 (37) (2014) 7182–7194.
[35] W. Li, Y. Xu, G. Zhang, F. Qiu, Y. Yang, A.-C. Shi, Real-space self-consistent mean-field theory study of ABC star triblock copolymers, J. Chem. Phys. 133 (6) (2010), 064904.
[36] P. Tang, F. Qiu, H. Zhang, Y. Yang, Morphology and phase diagram of complex block copolymers: ABC linear triblock copolymers, Phys. Rev. 69 (3) (2004), 031803.
[37] G. Zhang, F. Qiu, H. Zhang, Y. Yang, A.-C. Shi, SCFT study of tiling patterns in ABC star terpolymers, Macromolecules 43 (6) (2010) 2981–2989.
[38] K. Aissou, H.K. Choi, A. Nunns, I. Manners, C.A. Ross, Ordered nanoscale archimedean tilings of a templated 3-miktoarm star terpolymer, Nano Lett. 13 (2) (2013) 835–839.
[39] K. Aissou, W. Kwon, M. Mumtaz, S. Antoine, M. Maret, G. Portale, G. Fleury, G. Hadziioannou, Archimedean tilings and hierarchical lamellar morphology formed by semicrystalline miktoarm star terpolymer thin films, ACS Nano 10 (4) (2016) 4055–4061.
[40] H.K. Choi, A. Nunns, X.Y. Sun, I. Manners, C.A. Ross, Thin film knitting pattern morphology from a miktoarm star terpolymer, Adv. Mater. 26 (16) (2014) 2474–2479.
[41] S. Chernyy, J.J.K. Kirkensgaard, J.P. Mahalik, H. Kim, M.M.L. Arras, R. Kumar, B. G. Sumpter, G.S. Smith, K. Mortensen, T.P. Russell, K. Almdal, Bulk and surface morphologies of ABC miktoarm star terpolymers composed of PDMS, PI, and PMMA arms, Macromolecules 51 (3) (2018) 1041–1051.
[42] S. Chernyy, J.P. Mahalik, R. Kumar, J.J.K. Kirkensgaard, M.M.L. Arras, H. Kim, L. Schulte, S. Ndoni, G.S. Smith, K. Mortensen, B.G. Sumpter, T.P. Russell, K. Almdal, On the morphological behavior of ABC miktoarm stars containing poly (cis 1,4-isoprene), poly(styrene), and poly(2-vinylpyridine), J. Polym. Sci. B Polym. Phys. 56 (22) (2018) 1491–1504.
[43] S. Lee, L.-C. Cheng, K.G. Yager, M. Mumtaz, K. Aissou, C.A. Ross, In situ study of ABC triblock terpolymer self-assembly under solvent vapor annealing, Macromolecules 52 (4) (2019) 1853–1863.
[44] Y. Bohbot-Raviv, Z.-G. Wang, Discovering new ordered phases of block copolymers, Phys. Rev. Lett. 85 (16) (2000) 3428–3431.
[45] W. Li, F. Qiu, A.-C. Shi, Emergence and stability of helical superstructures in ABC triblock copolymers, Macromolecules 45 (1) (2012) 503–509.
[46] M. Liu, W. Li, F. Qiu, A.-C. Shi, Theoretical study of phase behavior of frustrated ABC linear triblock copolymers, Macromolecules 45 (23) (2012) 9522–9530.
[47] C.A. Tyler, D.C. Morse, Orthorhombic network in triblock and diblock copolymer melts, Phys. Rev. Lett. 94 (20) (2005), 208302.
[48] K. Ueda, T. Dotera, T. Gemma, Photonic band structure calculations of two-dimensional Archimedean tiling patterns, Phys. Rev. B 75 (19) (2007), 195122.
[49] A. Arora, J. Qin, D.C. Morse, K.T. Delaney, G.H. Fredrickson, F.S. Bates, K. D. Dorfman, Broadly accessible self-consistent field theory for block polymer materials discovery, Macromolecules 49 (13) (2016) 4675–4690.
[50] F.S. Bates, M.A. Hillmyer, T.P. Lodge, C.M. Bates, K.T. Delaney, G.H. Fredrickson, Multiblock polymers: panacea or pandora's box? Science 336 (6080) (2012) 434.
[51] T. Gemma, A. Hatano, T. Dotera, Monte Carlo simulations of the morphology of ABC star polymers using the diagonal bond method, Macromolecules 35 (8) (2002) 3225–3237.
[52] W. Xu, K. Jiang, P. Zhang, A.-C. Shi, A strategy to explore stable and metastable ordered phases of block copolymers, J. Phys. Chem. B 117 (17) (2013) 5296–5305.
[53] K. Hayashida, W. Kawashima, A. Takano, Y. Shinohara, Y. Amemiya, Y. Nozue, Y. Matsushita, Archimedean tiling patterns of ABC star-shaped terpolymers studied by microbeam small-angle X-ray scattering, Macromolecules 39 (14) (2006) 4869–4872.
[54] K. Hayashida, A. Takano, S. Arai, Y. Shinohara, Y. Amemiya, Y. Matsushita, Systematic transitions of tiling patterns formed by ABC star-shaped terpolymers, Macromolecules 39 (26) (2006) 9402–9408.
[55] A. Takano, W. Kawashima, A. Noro, Y. Isono, N. Tanaka, T. Dotera, Y. Matsushita, A mesoscopic Archimedean tiling having a new complexity in an ABC star polymer, J. Polym. Sci. B Polym. Phys. 43 (18) (2005) 2427–2432.
[56] A. Takano, S. Wada, S. Sato, T. Araki, K. Hirahara, T. Kazama, S. Kawahara, Y. Isono, A. Ohno, N. Tanaka, Y. Matsushita, Observation of cylinder-based microphase-separated structures from ABC star-shaped terpolymers investigated by electron computerized tomography, Macromolecules 37 (26) (2004) 9941–9946.
[57] S. Sioula, Y. Tselikas, N. Hadjichristidis, Synthesis of model 3-miktoarm star terpolymers of styrene, isoprene, and methyl methacrylate, Macromolecules 30 (5) (1997) 1518–1520.
[58] S. Sioula, N. Hadjichristidis, E.L. Thomas, Direct evidence for confinement of junctions to lines in an 3 miktoarm star terpolymer microdomain structure, Macromolecules 31 (23) (1998) 8429–8432.
[59] S. Sioula, N. Hadjichristidis, E.L. Thomas, Novel 2-dimensionally periodic non-constant mean curvature morphologies of 3-miktoarm star terpolymers of styrene, isoprene, and methyl methacrylate, Macromolecules 31 (16) (1998) 5272–5277.
[60] M. Farré, D. Barceló, Chapter 1 - introduction to the analysis and risk of nanomaterials in environmental and food samples, in: M. Farré, D. Barceló (Eds.), Comprehensive Analytical Chemistry, Elsevier, 2012, pp. 1–32.
[61] S. Ndoni, C.M. Papadakis, F.S. Bates, K. Almdal, Laboratory-scale setup for anionic polymerization under inert atmosphere, Rev. Sci. Instrum. 66 (2) (1995) 1090–1095.
[62] A.K. Khandpur, S. Foerster, F.S. Bates, I.W. Hamley, A.J. Ryan, W. Bras, K. Almdal, K. Mortensen, Polyisoprene-polystyrene diblock copolymer phase diagram near the order-disorder transition, Macromolecules 28 (26) (1995) 8796–8806.
[63] F.S. Bates, J.H. Rosedale, H.E. Bair, T.P. Russell, Synthesis and characterization of a model saturated hydrocarbon diblock copolymer, Macromolecules 22 (6) (1989) 2557–2564.
[64] A.P. Hammersley, S.O. Svensson, M. Hanfland, A.N. Fitch, D. Hausermann, Two-dimensional detector software: from real detector to idealised image or two-theta scan, High Pres. Res. 14 (4–6) (1996) 235–248.
[65] B.R. Pauw, Everything SAXS: small-angle scattering pattern collection and correction, J. Phys. Condens. Matter 25 (38) (2013), 383201.
[66] Version 1. Natick, Curve Fitting Toolbox : for Use with MATLAB® : Users Guide, MathWorks, MA, 2001, 2001.
[67] C.A. Schneider, W.S. Rasband, K.W. Eliceiri, NIH Image to ImageJ: 25 years of image analysis, Nat. Methods 9 (7) (2012) 671–675.
[68] M.B.a.G. Andersson, GenX: an extensible X-ray reflectivity refinement program utilizing differential evolution, J. Appl. Crystallogr. 40 (6) (2007) 5.
[69] L.J. Fetters, D.J. Lohse, D. Richter, T.A. Witten, A. Zirkel, Connection between polymer molecular weight, density, chain dimensions, and melt viscoelastic properties, Macromolecules 27 (17) (1994) 4639–4647.

[70] H.B. Eitouni, N.P. Balsara, Thermodynamics of polymer blends, in: M.E. James (Ed.), Physical Properties of Polymers Handbook, Springer Science+Business Media, LLC, NewYork, 2007, pp. 339–356.
[71] O. Tcherkasskaya, S. Ni, M.A. Winnik, Direct energy transfer studies of the Domain−Boundary interface in Polyisoprene−Poly(methyl methacrylate) block copolymer films, Macromolecules 29 (2) (1996) 610–616.
[72] C.M. Papadakis, K. Almdal, K. Mortensen, D. Posselt, Identification of an intermediate-segregation regime in a diblock copolymer system, Europhys. Lett. 36 (4) (1996) 289–294.
[73] T. Hashimoto, T. Kawamura, M. Harada, H. Tanaka, Small-angle scattering from hexagonally packed cylindrical particles with paracrystalline distortion, Macromolecules 27 (11) (1994) 3063–3072.
[74] M.S. Tureau, W.-F. Kuan, L. Rong, B.S. Hsiao, T.H. Epps, Inducing order from disordered copolymers: on demand generation of triblock morphologies including networks, Macromolecules 45 (11) (2012) 4599–4605.
[75] M.S. Tureau, L. Rong, B.S. Hsiao, T.H. Epps, Phase behavior of neat triblock copolymers and copolymer/homopolymer blends near network phase windows, Macromolecules 43 (21) (2010) 9039–9048.
[76] M.S. Tureau, T.H. Epps III, Effect of partial hydrogenation on the phase behavior of poly(isoprene-b-styrene-b-methyl methacrylate) triblock copolymers, Macromolecules 45 (20) (2012) 8347–8355.
[77] R. Hiorns, Polymer handbook, 0-471-16628-6, in: fourth ed., in: J. Brandup, E. H. Immergut, E.A. Grulke, A. Abe, D.R. Bloch (Eds.), Polymer International, vol. 49, John Wiley and Sons, New York, 1999, p. 2250, 7) (2000) 807-870.
[78] Y.S. Jung, C.A. Ross, Orientation-controlled self-assembled nanolithography using a Polystyrene−Polydimethylsiloxane block copolymer, Nano Lett. 7 (7) (2007) 2046–2050.
[79] W.A.J. Zisman, N.L. Fox, R. B, Contact angle, wettability and adhesion, Adv. Chem. 43 (1964) 317–340.
[80] G. Krausch, Surface induced self assembly in thin polymer films, Mater. Sci. Eng. R Rep. 14 (1) (1995) 1–94.
[81] Y. Matsushita, Creation of hierarchically ordered nanophase structures in block polymers having various competing interactions, Macromolecules 40 (4) (2007) 771–776.
[82] B. Tonpheng, J. Yu, B.M. Andersson, O. Andersson, Tensile strength and Young's modulus of polyisoprene/single-wall carbon nanotube composites increased by high pressure cross-linking, Macromolecules 43 (18) (2010) 7680–7688.
[83] C. Ishiyama, Y. Higo, Effects of humidity on Young's modulus in poly(methyl methacrylate), J. Polym. Sci. B Polym. Phys. 40 (5) (2002) 460–465.
[84] I. Oral, H. Guzel, G. Ahmetli, Measuring the Young's modulus of polystyrene-based composites by tensile test and pulse-echo method, Polym. Bull. 67 (9) (2011) 1893–1906.
[85] M. Vayer, A. Guliyeva, F. Warmont, A. Takano, Y. Matsushita, C. Sinturel, Transition between tetragonal and hexagonal pattern in binary blends of ABC block copolymers with different chain lengths, Eur. Polym. J. 138 (2020), 109986.
[86] H. Nakazawa, T. Ohta, Microphase separation of ABC-type triblock copolymers, Macromolecules 26 (20) (1993) 5503–5511.
[87] D. Hurley, B. Ohler, White Paper: characterizing the atomic lattices of 2D crystals with AFM, MRS Bull. 42 (2) (2017) 89–90.
[88] J. Zhang, D. Posselt, A. Sepe, X. Shen, J. Perlich, D.-M. Smilgies, C.M. Papadakis, Structural evolution of perpendicular lamellae in diblock copolymer thin films during solvent vapor treatment investigated by grazing-incidence small-angle X-ray scattering, Macromol. Rapid Commun. 34 (16) (2013) 1289–1295.
[89] X. Zhang, K.G. Yager, S. Kang, N.J. Fredin, B. Akgun, S. Satija, J.F. Douglas, A. Karim, R.L. Jones, Solvent retention in thin spin-coated polystyrene and poly (methyl methacrylate) homopolymer films studied by neutron reflectometry, Macromolecules 43 (2) (2010) 1117–1123.